UC Berkeley

UC Berkeley Previously Published Works

Title

Exposing the Role of Electron Correlation in Strong-Field Double Ionization: X-ray Transient Absorption of Orbital Alignment in Xe+ and Xe2+

Permalink

https://escholarship.org/uc/item/5tr604hm

Journal

The Journal of Physical Chemistry A, 118(37)

ISSN

1089-5639

Authors

Sayres, Scott G
Hosler, Erik R
Leone, Stephen R

Publication Date

2014-09-18

DOI

10.1021/jp503468u

Peer reviewed

eScholarship.org Powered by the California Digital Library
University of California

THE JOURNAL OF PHYSICAL CHEMISTRY A

Article

pubs.acs.org/JPCA

Exposing the Role of Electron Correlation in Strong-Field Double Ionization: X-ray Transient Absorption of Orbital Alignment in Xe^+ and Xe^{2+}

Scott G. Sayres, Erik R. Hosler, and Stephen R. Leone*

Departments of Chemistry and Physics, University of California at Berkeley, Berkeley, California 94720, United States
Chemical Sciences Division, Lawrence Berkeley National Laboratory, Berkeley, California 94720, United States

ABSTRACT: Orbital alignment measurements and theory are used to examine the role of electron correlation during atomic strong-field double ionization (795 nm, (1−5) × 10^{14} W cm^{-2}). High-order harmonic, transient absorption spectroscopy is used to measure the angular distributions of singly and doubly tunnel-ionized xenon atomic states via 4d core to 5p valence shell transitions between 55 and 60 eV. The experimental M_J alignment distributions are compared to results of a rate-equation model based on sequential ionization, previously developed for coherent electron motion, and now applied to account for the alignment prepared by tunneling ionization. The hole generated in the $^2P_{3/2}$ state of Xe^+ is measured to be entirely composed of $|M_J|$ = 1/2, in agreement with theory. The result is a higher degree of alignment than previously reported. Because the model neglects effects of electron−ion recollision, the theory predicts a high degree of alignment in both spin-parallel (triplet) and antiparallel (singlet) terms of Xe^{2+}. However, the alignment generated with linearly polarized light is observed to be spin-state dependent. The measured alignments for triplet spin states ($^3P_2$ has $|M_J|$ = [0 : 1 : 2] of [27±6 : 45±11 : 29±0] and $^3P_1$ has $|M_J|$ = [0 : 1] of [56±2 : 44±2]) are in good agreement with the expectations of theory, which are [33 : 53 : 14] and [66 : 33], respectively. The results validate the rate equation model for sequential tunnel ionization. However, the alignment extracted for a singlet state is greatly diminished: $^1D_2$ is measured to be [18±1 : 39±2 : 43 ± 2] compared to theoretical expectation of [60 : 39 : 1] for $|M_J|$ = [0 : 1 : 2]. The poor agreement with the sequential ionization model suggests that the alignment of $^1D_2$ is strongly influenced by the high propensity for the liberated first electron to return to and recollide with its parent atomic orbital. Therefore, although the influence of electron recollision appears minor in the triplet states and suggests sequential ionization, electron correlation between the ionic core and the first ionized electron cannot be ignored in the singlet state. Singlet states are likely to be generated through nonsequential double ionization over the intensity range where the experiments are performed.

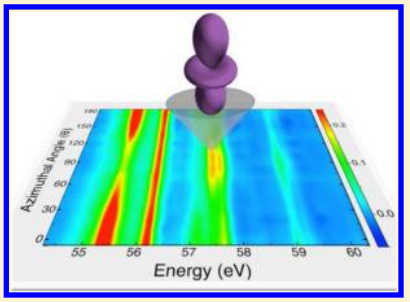

I. INTRODUCTION

Strong-field ionization (SFI) is the birthing process for electrons involved in many important physical phenomena including high-harmonic-generation (HHG),[1] attosecond pulse generation,[2] orbital tomography,[3,4] and novel forms of lithography.[5] It is also considered to be a promising route for launching and observing nonstationary electron dynamics in both atoms[6] and molecules,[7] as well as vibrational coherences.[8] Knowledge of the SFI processes is progressing rapidly, but it is still far from being entirely understood, especially under conditions where electron correlation is strong. As such, advances in the frontier of electron correlation will be universally applicable to the ultrafast community.

Noble gases remain a preferred target of both theoreticians and experimentalists, having inert and closed p shells, which give good agreement with the well-known single active electron tunneling rate equations, such as the Ammosov−Delone−Krainov (ADK) model.[9] The appearance of singly charged ions is often understood by ADK predictions, even in complicated polyatomic systems such as clusters.[10,11] However, multiple or even double ionization presents a significant challenge due to electron correlation (interaction) effects. Electron correlation has become one of the most important frontiers in strong-field light−matter interactions,[12] where many experimental observations cannot be understood by assuming independent electrons. The influence of electron correlation is commonly observed in the angular distribution of photoelectrons,[13] in HHG,[14,15] most prominently in nonsequential double ionization (NSDI),[16] and even in sequential ionization.[17,18] The influence of electron correlation on alignment, defined as a nonuniform M_J distribution of the final ion states, remains unexplored.

Conventional experimental approaches, such as the measurement of ion yields versus laser intensity,[19,20] have been seminal in understanding how the ionization potential (IP) and angular momentum affects the ionization rate; however, they do not provide information on the ion states and alignment following ionization. Only recently have techniques emerged that directly

Special Issue: A. W. Castleman, Jr. Festschrift

Received: April 8, 2014
Revised: June 6, 2014
Published: June 9, 2014

 © 2014 American Chemical Society dx.doi.org/10.1021/jp503468u | J. Phys. Chem. A 2014, 118, 8614−8624

explore the quantum state distribution of the hole in the resulting ion. X-ray core-level absorption spectroscopy gives a unique perspective to directly observe the final ion states,[21,22] and the method using laser-produced high harmonics in the extreme ultraviolet (XUV) has become a powerful technique for measuring the states and alignment produced in the SFI of noble gas atoms. Pioneering works examining the SFI dynamics of noble gas atoms by core-level transitions to the vacancy in the valence state have demonstrated that ion alignment occurs because of vastly different ionization rates of the valence electrons.[22,23] In the absence of spin−orbit coupling, the electrons aligned with the laser field (orbital angular momentum quantum number, $m_l = 0$) have much higher ionization rates compared to the states that are not aligned with the field ($m_l = 1$). Multiple experiments have demonstrated that the degree of alignment during ion formation resulting from the SFI of noble gases,[6,16,17] and specifically xenon,[23,24] is less than predicted by theoretical models.[25,26] Even similar laser pulses can generate different values, demonstrating that the generated alignment is highly sensitive to laser parameters, such as pulse width, intensity, and temporal profile. Generally, longer pulses seem to provide better agreement, but further work is needed to account for the diminished alignment that may be due to electron−ion recollision or other multielectronic effects during ionization. Electronic wave packets have also been prepared and examined in atoms with attosecond temporal resolution,[6,27] demonstrating that the single active electron approximation is generally accurate in describing single ionization.

NSDI is important in linearly polarized laser experiments, where doubly charged ions are generated through enhanced ionization by recollision at or below the threshold for sequential tunneling ionization.[16] NSDI is described by the semiclassical three-step model.[1] First, the valence electron aligned with the laser polarization tunnels according to a static field ionization rate and the remaining electrons are treated using a frozen core approximation. Second, the liberated electron is assigned zero kinetic energy and is treated classically as it interacts with the laser field. Upon reversal of the electric field of the laser, the liberated electron returns to its parent orbital. In the third step, the ion-electron impact occurs with sufficient kinetic energy to remove a second electron or generate a harmonic photon. Many-electron effects are generally ignored in this simple model. The first two steps are quite well understood to be entirely spin independent; however, it has recently been shown that additional information can be extracted about two-electron dynamics from the HHG spectrum if spin were accounted for in the third step.[15,28]

Upon double ionization, the two holes in the valence shell interact and influence each other's motion. The two holes are generated with spins aligned either parallel (triplet states) or antiparallel (singlet states) and having very different spatial distributions. The interaction of the electrons in the Xe^{2+} states influences the electron−ion recollision probability. Here, we address whether the measurements of orbital alignment prepared in each spin state of Xe^{2+} through SFI can reveal the role of spin state on electron−ion recollision. It is to this end that core-level absorption spectroscopy is used to determine the alignment of the valence shell holes prepared through the strong-field double ionization of Xe. In a recent publication, a rate equation model was developed to address the coherences that can be generated and observed in singly and doubly ionized states through sequential SFI.[29] Here, this model is applied to interpret the alignment of both triplet and singlet states resulting from the strong-field double ionization of xenon. Direct comparison between the experimental alignments for the triplet and singlet states and the sequential ionization model allows us to address fundamental questions regarding the influence of electron−ion recollision on ion alignment prepared through SFI.

II. EXPERIMENTAL METHODS

The extreme ultraviolet (XUV) transient absorption spectroscopy instrument has been described previously.[30] A commercial 800 nm femtosecond laser system with center wavelength of 795 nm, producing 2.8 mJ, 40 fs pulses at 1 kHz repetition rate, is split into two beams and then recombined on a sample with defined time delay. One pulse is used to ionize the sample of Xe atoms by SFI [$(1-5) \times 10^{14}$ W/cm^2] and the other pulse generates high harmonics for absorption measurements. The XUV probe pulse is produced via even/odd high harmonic generation utilizing a semi-infinite gas cell configuration and a two color laser field of 1.6 mJ:25 μJ of 800:400 nm light, respectively. Two 600 nm thick Al foils between the Ne-containing high harmonic semi-infinite gas cell and the refocusing toroidal mirror remove the residual NIR and visible pulses. This configuration provides a quasi-continuous XUV spectrum from ∼40 to 72.5 eV (Al filter $N_{2,3}$ edge), with bright 0.2 eV bandwidth harmonics spaced by 1.5 eV and <10:1 peak-to-valley harmonic:continuum ratio. The 795 nm strong-field pump beam is focused into the target Xe cell by a 45 cm focal length lens yielding a focal beam waist radius (w_0) of 32 μm. A half-wave plate and thin-film plate polarizer pair control the laser intensity while preserving spatial parameters. The pump volume sampled by the smaller XUV probe ($w_0 = 22 \pm 2$ μm) means that the ionized Xe density varies less than 5% from its peak value due to the spatial profile of the pump beam. The strong-field pump (40 fs, 125−450 μJ) is overlapped with the XUV probe at a 1° crossing angle in the target gas cell (200 μm entrance and exit apertures and 4 mm path length). A 200 nm thick Al foil positioned at the entrance of the XUV spectrometer prevents the 795 nm pump beam from reaching the detector.

Following the single or double ionization of atomic xenon by the pump pulse, the probe laser pulse interrogates the produced state distribution by monitoring the transition probability along its own polarization. The probe pulse transfers electron population from the 4d core to the 5p hole(s), and the cross section for absorption varies with polarization due to alignment of the prepared hole(s). An energy diagram representation of this process is presented in Figure 1. Polarization-dependent transient absorption spectra are obtained by collecting XUV pump−probe spectra as a function of the polarization angle of the pump varied relative to the probe beam at a fixed time delay of 500 fs. The polarization of the strong-field pump is rotated with a half-wave plate and polarizer with 10^4 extinction ratio. The absorption cross-section was monitored while the polarization angle between the pump and probe laser pulses was scanned in 10° increments between 0° and 180°. From the anisotropy of the core-level absorption, the alignment parameters are extracted.

Each absorption spectrum is referenced to an individual "pump-off" spectrum. The transient absorbance (optical density) is defined as, $\Delta OD(E,t) = -\log[I(E,t)/I(E,\text{"pump-off"})]$, where $I(E,t)$ is the spectral intensity of the XUV light at a photon energy, E, and time delay, t, and $I(E,\text{"pump-off"})$ is measured in the absence of the pump beam. Transient

dx.doi.org/10.1021/jp503468u | J. Phys. Chem. A 2014, 118, 8614−8624

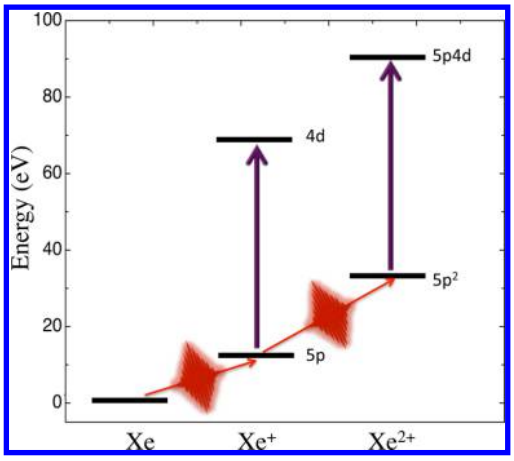

Figure 1. Average energies of the Xe configurations relevant to this experiment. The X-ray transitions are shown as vertical arrows and the tunneling (pump) laser transitions in the horizontal direction. Although the tunneling laser is shown as two pulses to represent sequential ionization, the double ionization occurs in one laser pulse. The notation nl^x is used to represent the angular momentum quantum numbers of the hole(s).

absorption spectra represent an average of 128 spectra, with a CCD integration time of 0.2 s for each spectrum, and give a total of 25.6 thousand laser pulses accumulated per spectra. The absorption spectrum for perpendicular laser pulses at high intensity (5×10^{14} W/cm^2) is presented in Figure 2, where

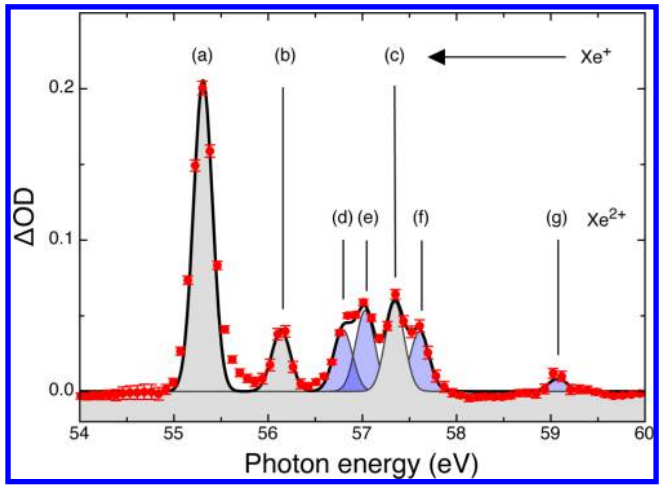

Figure 2. Transient absorption spectra at a time delay of 500 fs showing the Xe^+ and Xe^{2+} core−hole absorptions taken with perpendicular polarized laser pulses to enhance the observation of peaks (c, f, and g). The red circles represent data points, and error bars correspond to one standard error of the mean of the measured value. The laser intensity is estimated to be 5×10^{14} W/cm^2. Resonances attributed to singly charged ions are highlighted in gray, and doubly charged resonances are highlighted in blue. Labels: (a) $^2P_{3/2} \rightarrow {}^2D_{5/2}$, (b) $^2P_{1/2} \rightarrow {}^2D_{3/2}$, (c) $^2P_{3/2} \rightarrow {}^2D_{3/2}$, (d) $^3P_2 \rightarrow {}^1D_2$, (e) $^3P_2 \rightarrow {}^3D_3$, (f) $^1D_2 \rightarrow {}^1F_3$ and $^3P_1 \rightarrow {}^3D_2$, and (g) $^3P_1 \rightarrow {}^3D_1$.

absorption peaks are attributed to both Xe^+ and Xe^{2+}. Spin−orbit splitting in both the valence (p) and core (d) shells of Xe^+ allows for four possible $d^{10}p^5 \rightarrow d^9p^6$ transitions. Selection rules limit the absorption spectra to three peaks ($^2P_{1/2,1/2} \rightarrow {}^2D_{5/2}$ is forbidden). The Xe^{2+} $d^{10}p^4 \rightarrow d^9p^5$ has a rich absorption spectrum, where 5 terms exist in the valence shell (p^4) and 12 terms exist in d^9p^5. Within this electronic transition, theory predicts 34 allowed transitions[31] having varying oscillator strengths, and spanning a range of ∼10 eV that overlaps the Xe^+ $d^{10}p^5 \rightarrow d^9p^6$ transitions. The observed spectrum is in agreement with photoelectron spectra, and therefore, peaks are assigned according to previous literature sources.[31,32] We observe four XUV core to valence state dication absorption resonances, which allow for the full characterization of alignment in all Xe^{2+} terms. Two transitions originate from $^3P_2$, one from $^3P_1$, and one peak involves an overlap of both $^3P_1$ and $^1D_2$.

The instrumental XUV spectral resolution is 214 ± 15 meV, as determined by a least-squares fit of Voigt profiles to the 4d to 6p and 7p Rydberg states of Xe.[33] The instrumental response, defined by the rise time of the Xe^+ $^2P_{3/2} \rightarrow {}^2D_{5/2}$ transition at 55.4 eV, is 33 ± 6 fs. Zero time-delay (t = 0 fs) is defined as the center of the rise. Positive time delay corresponds to a pulse sequence where the XUV pulse train arrives after the strong-field pump pulse. Here, the SFI pulse is much longer than the time scale determined by the valence shell splitting; this means only diagonal elements of the density matrix remain populated after the pulse and simplifies the measurement and interpretation by eliminating any time-dependent coherent oscillations. Indeed, we observe no modulation in the angular distributions as a function of time delay, and a time delay of 500 fs is arbitrarily used for measuring the anisotropy.

Removal of both electrons is accomplished within the same linearly polarized pulse, imposing cylindrical symmetry (there is no orientation, meaning $\pm M_J$ substates are equally populated), which restricts the multipoles that can be measured. Because the laser beams copropagate, absorption is sensitive to only the diagonal even elements of the density matrix. The absorption cross section of the probe pulse simplifies to a function of θ, the angle between the quantization axis (defined by the polarization direction of the pump laser), and the polarizing vector of the sampling XUV pulse. The absorption anisotropy is fit with the well-known multipole expansion:

$$I(\theta) = \frac{\sigma}{4\pi}[1 + \beta_2 P_2(\cos\theta) + \beta_4 P_4(\cos\theta) + ...] \quad (1)$$

where σ is the integral cross section, $P_{2,4}$ are Legendre polynomials, and β_2 and β_4 are the second-order (k = 2) and fourth-order (k = 4) anisotropy parameters, respectively. The expansion must be performed out to the number of terms equal to the maximum J value to accurately determine alignment. In Xe^+, where $J < 2$, the system is limited to β_2, and alignment can be determined using the absorption at only two angles. Alignment is commonly reported as $R = (I^{\parallel} - I^{\perp})/(I^{\parallel} + 2I^{\perp})$, where $I^{\parallel}$ and $I^{\perp}$ represent the absorptions at 0° and 90°, respectively. As term symbols for Xe^{2+} range up to J = 2, β_4 terms can exist and a minimum of three absorption measurements taken at different angles are required for the reconstruction. It is therefore appropriate to describe the anisotropy with eq 1. This method of reporting alignment fully represents the angular distribution and is directly comparable to previous anisotropy measurements (conversion to the commonly reported alignment parameter is $\beta_2 = 2R$). Extracting the β values from the raw data allows for the reconstruction of the resultant magnetic substate distribution or alignment.

III. THEORETICAL METHODS

III.A. Tunneling Ionization. SFI is often described by the single active electron approximation,[9] where the ionization rate,

dx.doi.org/10.1021/jp503468u | J. Phys. Chem. A 2014, 118, 8614−8624

and thus angular response, is proportional to the density of the active electron in the direction of the laser polarization. The static-field tunneling rate, W_{TI}, equation[34] used herein is a modified version of the standard ADK model, accounting for the barrier suppression region:

$$W_{TI}(F) = \frac{C_l^2}{2^{|m_l|}|m_l|!}\frac{(2l+1)(l+|m_l|!)}{2(l-|m_l|!)}\frac{1}{k_e^{2Z_c/k_e-1}} \times \left(\frac{2k_e^3}{F}\right)^{2Z_c/k_e-|m_l|-1} e^{-2k_e^3/3F} e^{-\alpha(Z_c^2/IP)(F/k_e^3)} \quad (2)$$

where $k_e = (2IP)^{1/2}$, F is the electric field amplitude, Z_c is the effective nuclear charge, and l and m_l are the angular momentum quantum numbers. The rate is dependent upon the parameters used and are specific for each atom (here, α = 15, C_l = 2.27); however, as these parameters are maintained for all states of equal charge, they do not significantly influence the population distribution (atomic units: $\hbar = m_e = e = 1$ are utilized within this manuscript unless otherwise noted). Numerical integration over the ionizing laser pulse is needed, where the static ionization rates from eq 2 vary in time with the oscillating electric field of the laser.

Application of the tunneling rate expressed in eq 2 requires the IP and single electron angular momentum quantum numbers to be well-defined. Due to spin−orbit coupling, there is no basis set that describes these values simultaneously. In the coupled basis (JM_J), energy is well-defined but the angular momentum of individual electrons is not. In contrast, individual electron orbitals are well-defined in the uncoupled basis (ls), but their binding energy is not. Recently, we developed a model[29] for describing the sequential tunnel ionization of noble gas atoms and obtained satisfactory agreement with ab initio calculations[21] for both the ion M_J-state distributions and the coherences between states in the singly charge ion. Within this model, ionization rates are determined in the conversion matrix, where each element is assigned well-defined l and m_l angular momentum numbers as well as binding energies, thereby allowing application of eq 2. Once the conversion matrix is populated, transformation to either (ls) or (JM_J) basis notation reveals their respective populations. In the (ls) basis, the single electron wave functions ($\psi_{lm_lsm_s}$) are described by standard spherical harmonics (Y_{lm_l}). The conversion between (JM_J) and (ls) basis for a singly charged ion for constructing the conversion matrix is

$$\psi_{JM_J} = \sum_{m_l m_s} C(lsm_l m_s; jm_j)\psi_{lm_l sm_s} \quad (3a)$$

$C(j_1 j_2 m_1 m_2; j_3 m_3)$ is a Clebsch−Gordan coupling coefficient used as scalar in a linear combination of wave functions describing a basis transformation, where lowercase letters (l = 1, s = 1/2, j) represent the orbital, spin, and total angular momentum quantum numbers that denote symmetry of an individual hole, and m_x are their projections from the quantization axis. Two electron wave functions can be constructed from linear combinations of bipolar spherical harmonic functions:[35]

$$\psi_{JM_J}^{ab} = \sum_{M_L M_S} C(LSM_L M_S; JM_J) \sum_{M_{l_1} M_{l_2}} C(l_1 l_2 m_{l_1} m_{l_2}; LM_L) \times \sum_{m_{s_1} m_{s_2}} C(s_1 s_2 m_{s_1} m_{s_2}; SM_s)\psi_{l_1 m_{l_1} s_1 m_{s_1}}\psi_{l_2 m_{l_2} s_2 m_{s_2}} \quad (3b)$$

where a and b represent the spatial coordinates of the first and second electron. Within LS coupling, where L and S are coupled to a total angular momentum vector **J**, the capital letters (L, S, J and their projections M_L, M_S, M_J) represent the total angular momentum quantum numbers of the atom. The central field approximation, where each electron experiences an effectively spherical potential, assumes the wave function to be a product of independent one-electron orbitals thereby ignoring electron correlation. Applying the Hartree−Fock method (expressing the wave function as a single Slater determinant) generates an antisymmetric wave function, as required by the Pauli principle. Antisymmetrizing by means of coordinate exchange gives the LS-coupled wave functions:[35]

$$\psi_{JM_J} = 2^{1/2}(\psi_{JM_J}^{ab} - \psi_{JM_J}^{ba}) \quad (4)$$

SFI prepares off diagonal density matrix elements in both (ls) and (JM_J) representations, indicating the formation of a coherent superposition between two electronic states. The spatial arrangement of the hole exhibits periodic movement according to the difference in energy between populated states, which is evaluated with the von Neumann equation. In Xe^+, the energy splitting of the valence shell (1.3 eV) gives a period of 3.2 fs, which is nearly resonant with the period of the fundamental driving laser frequency (2.7 fs). Consequently, this rapid motion redistributes the hole population among the (ls) states. The Xe^+ ensemble's hole distributions oscillate between peanut and donut geometries as constructed from the diagonal elements of the (ls) basis.[6] This coherent electron motion of the ensemble, represented by the off diagonal density matrix elements, influences the sequential ionization rate and is accounted for in the model.[29,36]

The onset of sequential ionization (defined as having 1% of the ions as Xe^{2+}) is 1.2 × 10^{14} W/cm^2, and the saturation intensity (where all ions are doubly ionized) is 2 × 10^{15} W/cm^2. After double ionization, the Xe^{2+} ions reside in either the ground term (^{3}P) or excited singlet states (^{1}D$_2$ or ^{1}S$_0$ are higher in energy by 2.1 and 4.5 eV, respectively).[37] It is reasonable to assume that because of the large difference in ionization rates, the second electron would also arise from m_l = 0 and therefore empty the p$_z$ orbital. However, laser intensity plays an important role in the resultant term distribution. Due to the exponential dependence of the tunneling rate on IP, triplet states are accessed at lower fields than singlets, and this indicates that electrons are removed from different atomic orbitals. The laser field can overcome the difference in IP for obtaining singlet states, and at an intensity of ∼3 × 10^{14} W/cm^2 the ionization rate for producing a ^{1}D$_2$ state is dominant where both electrons are m_l = 0 and thus ionization empties the p$_z$ orbital. The ^{1}S$_0$ population is negligible due to its larger IP. As laser intensity increases, the difference in energy between the states becomes less important, and population approaches the statistical distribution (^{3}P:^{1}D:^{1}S = 9:5:1) assuming sequential ionization. Triple ionization is not included in the theoretical model, as this does not occur until even higher intensities (∼1 × 10^{15} W/cm^2) for this pulse width.

dx.doi.org/10.1021/jp503468u | J. Phys. Chem. A 2014, 118, 8614−8624

Though the ratio between the populations of terms shows strong dependence on laser intensity, the energy degeneracy of the magnetic substates makes alignment nearly stable with respect to laser intensity. Large differences in ionization rates for the different pathways, obtained from the conversion matrix, are responsible for orbital alignment. The $^3P_{2,2}$ state arises from the removal of spin-parallel $m_l = 1$ and 0 electrons. Though the $m_l = 0$ electron is quickly removed, the $m_l = 1$ electron has a low ionization rate. For $^3P_1$, the channels for $M_J = 0$ have approximately double the rate of $M_J = 1$ channels. Alignment is predicted to be most extreme in the $^1D_2$ state, where the $^1D_{2,0}$ substate is comprised in large part by an empty p_z orbital and both electrons in p_z have a large ionization rate. In contrast, the $^1D_{2,2}$ and $^1D_{2,1}$ substates contain $m_l = 1$ electrons, thus limiting their production because of lower ionization rates.

III.B. Angular Cross Sections for XUV Photon Absorption. According to Fermi's golden rule, the absorption cross section of the XUV probe light is dependent on the angular momentum of the initial and final states as well as the angle between pump and probe polarization vectors as shown in eq 5. The Wigner rotation matrix, $d^l_{mm'}(\theta)$, describes the rotation of the photon's polarization.

$$I_{\mathrm{XUV}}(\theta) = |\langle\psi_f|\sum_{m'} d^l_{mm'}(\theta)\mu|\psi_i\rangle|^2 \tag{5}$$

The final and initial states are represented by ψ_f and ψ_i. The dipole operator is related to spherical harmonics ($\mu \sim Y_{1,0} = r \times \cos(\theta)$), resulting in the integration over three spherical harmonic functions. Although the calculation for single photon absorption is obtained in the uncoupled basis through numerical integration, it is greatly simplified in the coupled basis using standard angular momentum algebra. The angular and radial components of the wave function are separated according to the Wigner–Eckart theorem.

$$|\langle JM_f|\mu|JM_i\rangle| = C(J_f 1M_f q; J_i M_i)|\langle J_f\|\mu\|J_i\rangle| \tag{6}$$

where j and m are the quantum numbers of the orbitals that denote symmetry of the hole. The Clebsch–Gordan coefficient contains all of the angular information from a single photon transition and describes the alignment. Within the Clebsch–Gordan coefficient, q represents the polarization vector of light with respect to the transition dipole moment or quantization axis, where $q = 0$ is for parallel polarized light and $q = \pm 1$ is for perpendicular polarized light. The reduced matrix element, expressed by $\langle J_f\|\mu\|J_i\rangle$, is not relevant to the discussion of alignment as it is independent of M_J, but these elements are useful for peak assignments. Reduced dipole matrix elements are obtained through the Flexible Atomic Code (FAC),[38] a relativistic multiconfigurational interaction method that yields Dirac–Fock energy levels and oscillator strengths.

The treatment[39] of alignment from multiphoton absorption[40] and fluorescence[41−43] is well-developed within perturbation theory. The spatial distribution of an electronic state can be expressed in terms of multipole expansion tensors of rank k and projections q, where ranks $k \leq 2J$ are allowed. The expectation of a rank k tensor depends only on the state multipole of the same rank. The quadrupolar (double-headed arrow with $k = 2$) nature of linearly polarized light limits single-photon absorption or fluorescence to only rank $k = 0$ (population), $k = 1$ (orientation), and $k = 2$ (alignment) observation, independent of the rank multipoles describing the spatial distribution of the state. Detecting higher moments requires multiple photons. Typically, multipole expansion requires a number of terms equal to the number of photons absorbed, but a more general description is the number of electronic transitions (these statements are equivalent in perturbation theory). From the atom's perspective, each individual electronic transition imparts rank $k \leq 2$ spatial anisotropy according to the angular-dependent transition probability, but through transformation into the laboratory frame observation, the absorption represents the multipole moments of all spectroscopic transitions combined (multiplied together prior to squaring). The higher order alignment components in the observed spectra versus angle, shown in Figure 3, indicates that the single-photon core-level XUV absorption carries a signature of SFI.

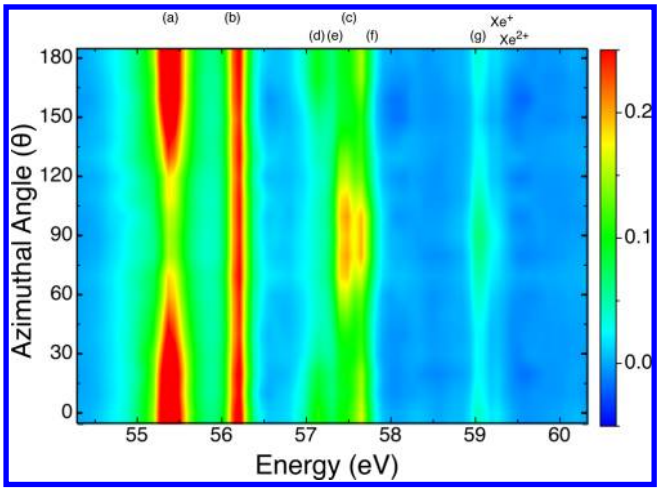

Figure 3. Contour plot of the relevant energy range showing the anisotropy of the Xe^+ and Xe^{2+} absorption features. The color scale is the change in optical density. It is immediately clear that the singly charged ions are represented fully by the alignment parameter, β_2, whereas the Xe^{2+} peaks require the inclusion of the second-order alignment parameter, β_4. Labels: (a) $^2P_{3/2} \rightarrow {}^2D_{5/2}$, (b) $^2P_{1/2} \rightarrow {}^2D_{3/2}$, (c) $^2P_{3/2} \rightarrow {}^2D_{3/2}$, (d) $^3P_2 \rightarrow {}^1D_2$, (e) $^3P_2 \rightarrow {}^3D_3$, (f) $^1D_2 \rightarrow {}^1F_3$ and $^3P_1 \rightarrow {}^3D_2$, and (g) $^3P_1 \rightarrow {}^3D_1$.

The perturbative foundation of multiphoton ionization is invalid for SFI, meaning a treatment for the observed anisotropy from the combined pulses requires further consideration. In the nonrelativistic limit, electric fields do not interact with the spin angular momentum vectors. Thus, the spatial distribution prepared through SFI is according to the orbital angular momentum vector **L**, and not the total angular momentum vector **J**, making it necessary to expand the multielectron wave function into the uncoupled basis where spin is decoupled and orbital angular momentum is well-defined. Although eq 2 accounts for ionization rates, the spatial anisotropy resulting from SFI requires that the bipolar spherical harmonic components of eq 3b be replaced by the atomic spherical harmonics, Y_{LM_L}. The SFI angular probability, and thus the ion's spatial distribution, is a summation over the component products of atomic spherical harmonics squared, $Y_{LM_L}{}^2$, and diagonal elements.[44−46] The laboratory frame observation requires each XUV transition to be weighted by the SFI angular probability, and it is performed in the uncoupled basis. The combined effect of the SFI response with the perturbative XUV response for determining the alignments in multiply charged states is

dx.doi.org/10.1021/jp503468u | J. Phys. Chem. A 2014, 118, 8614−8624

$$I_{JM_J}(\theta) = |\langle \sum_{(ls)_f} \psi_{(ls)_f} | \sum_{m'} d^J_{mm'}(\theta)\mu | \sum_{(ls)_i} \psi_{(ls)_i} \rangle (Y_{LM_L}{}^2(\theta))|^2 \quad (7)$$

Although J states are prepared coherently through SFI, the substates are incoherently populated (orthogonal) by the Hamiltonian (see the coupling matrices of our previous article[29]). This allows each substate to be treated independently, for the construction of a basis set to interpret the degree of alignment from absorption signal. The overall angular information is determined as

$$I_J(\theta) = \sum_{M_J} f_{M_J} I_{jM_J}(\theta) \quad (8)$$

where f_{M_J} are the fractional population coefficients of the substate distribution and are normalized ($\sum f_{M_J} = 1$). A summation over the final substates is required because they are not resolved.

IV. RESULTS

IV.A. Alignment in Singly Charged Ions, Xe^+. A closed shell, p^6, contains only a rank 0 tensor (population), which has equal probability of absorbing light in all directions. Therefore, the SFI ($p^6 \rightarrow p^5$) defines the quantization axis, becomes a scalar, and is uninteresting. Alignment is prepared in $^2P_{3/2}$, allowing the subsequent XUV absorption to exhibit anisotropy, β_2. The XUV absorption spectra for Xe^+ have been previously described and alignments measured.[23,24] The basis set and therefore the theoretical limits on anisotropy for the Xe^+ transitions are presented in Table 1. The $^2P_{3/2} \rightarrow {}^2D_{5/2}$ transition limits $\beta_2 \in [+0.20, -0.20]$, depending on the degree of alignment in $^2P_{3/2}$. At the Xe^+ saturation intensity (2×10^{14} W/cm^2), the model here predicts an alignment in $^2P_{3/2}$, M_J = [1/2 : 3/2] of [95 : 5] in close agreement with previous theoretical work.[23] Erosion of singly charged states exposed to laser intensities exceeding the threshold for sequential ionization increases the alignment of Xe^+. The mechanism is similar to the reason the states are aligned in the first place: different ionization rates and pathways to double ionization. The $^2P_{3/2,3/2}$ erodes faster than $^2P_{3/2,1/2}$, making the alignment approach unity with increasing laser intensity. According to the model, at 5×10^{14} W/cm^2 (~50% doubly ionized), the orbital alignment in $^2P_{3/2}$, M_J = [1/2 : 3/2] is predicted to increase to [97 : 3].

Table 1. Theoretical Basis Set for Describing a Single Photon Absorption and Determining the Alignment Distribution in Xe^+[a]

energy (eV)	transition	σ	β_2	β_4
54.3	$^2P_{1/2,1/2} \rightarrow {}^2D_{5/2}$	–	–	–
55.4	$^2P_{3/2,1/2} \rightarrow {}^2D_{5/2}$	0.60	0.20	–
55.4	$^2P_{3/2,3/2} \rightarrow {}^2D_{5/2}$	0.60	−0.20	–
56.1	$^2P_{1/2,1/2} \rightarrow {}^2D_{3/2}$	0.66	0.00	–
57.3	$^2P_{3/2,1/2} \rightarrow {}^2D_{3/2}$	0.066	−0.80	–
57.3	$^2P_{3/2,3/2} \rightarrow {}^2D_{3/2}$	0.066	0.80	–

[a]Forbidden parameters are shown as dashes. The dimensionless line strengths, σ, determined through numerical integration, do not express angular information but instead just the overall strength of the transition. For Xe^+, all angular information is expressed by β_2.

Exploring the angular distribution of Xe^+ at laser intensities below those associated with the production of Xe^{2+} results in agreement with the model. The relative experimental absorption cross sections versus angle for the XUV transitions attributed to Xe^+ are presented in Figure 4 and the anisotropy coefficients are tabulated in Table 2. At low intensity, 1×10^{14} W/cm^2, where double ionization is minimized, the anisotropy at 55.4 eV for $^2P_{3/2} \rightarrow {}^2D_{5/2}$ of $\beta_2 = 0.23 \pm 0.04$ is recorded, within error of the theoretical limit for this transition, and indicates strong alignment [+107±10 : −7±10]. However, the measured anisotropy at 55.4 eV becomes unreasonable at higher laser intensities for $^2P_{3/2} \rightarrow {}^2D_{5/2}$ with the appearance of doubly charged ions, where we record values of up to $\beta_2 = 0.70$ (not shown), far exceeding theoretical limitations from even perfect alignment for the transition $^2P_{3/2} \rightarrow {}^2D_{5/2}$. We attribute the deviation of this peak to the possible overlap of an unknown multiply charged XUV absorption.

Although the lowest intensity result is in close agreement with the theoretical model, similar experiments report a reduced alignment of [85±6.8 : 15±6.8][23] and [70±10 : 30±10].[24] The results presented herein are recorded at many polarization angles and therefore less subject to errors that may be associated with measurements at just two angles. It is, however, possible that processes responsible for the anomalously high anisotropy at higher intensities in the present experiment may be affecting the results even at the lower intensities. This seems unlikely because the signal at 55.4 eV is larger than that of any Xe^{2+} peaks by more than a factor of 30. The differences in alignment measurements for Xe^+ will be further addressed in the Discussion.

The transition at 56.2 eV is assigned to $^2P_{1/2} \rightarrow {}^2D_{3/2}$. Alignment cannot exist in the $^2P_{1/2}$ state, making the absorption isotropic ($\beta_2 = 0$). The anisotropy measurement is within error, $\beta_2 = -0.03 \pm 0.05$. The $^2P_{1/2} \rightarrow {}^2D_{3/2}$ transition remains well isolated from other transitions and remains isotropic ($\beta_2 < 0.05$) even at the highest laser intensities explored.

The line strength for $^2P_{3/2} \rightarrow {}^2D_{3/2}$ (57.3 eV) is an order of magnitude lower than that of $^2P_{3/2} \rightarrow {}^2D_{5/2}$ (55.4 eV), making observation more difficult. Alignment makes the peak more intense with perpendicularly polarized laser pulses. Due to this difference in line strength, the spectra recorded with perpendicular polarized pulses is shown in Figure 2, where both peaks are easily observed and the difference between these peaks is minimized due to alignment. As both peaks originate from the same term, $^3P_2$, the measured alignments should be in agreement. The theoretical limits for the anisotropy are larger for this peak, where $\beta_2 \in [-0.80, +0.80]$, making it more sensitive to alignment. A value of $\beta_2 = -0.59 \pm 0.04$ is obtained, suggesting an alignment of [87±3 : 13±3]. The agreement is acceptable with the alignment determined from the $^2P_{3/2} \rightarrow {}^2D_{5/2}$ transition. However, there is clearly a higher order angular structure from neighboring peaks that is contaminating the measurement, as shown in Figure 4c. Although the resolution of the instrument does not allow for the separation of the contaminating peaks, it is possible to resolve the contributions using the angular distribution. When the data points (0 to 20° and 160 to 180°) that are most affected by the overlapping Xe^{2+} peaks are omitted from the fitting procedure, an anisotropy of $\beta_2 = -0.80 \pm 0.04$ is obtained. This gives an alignment of [100±3 : 0±3], which matches the measurement at 55.4 eV for $^2P_{3/2} \rightarrow {}^2D_{5/2}$. As noted above, the near perfect alignment measured here for Xe^+ $^2P_{3/2}$ is in good agreement with theory but is also higher than previously measured under similar laser

dx.doi.org/10.1021/jp503468u | J. Phys. Chem. A 2014, 118, 8614−8624

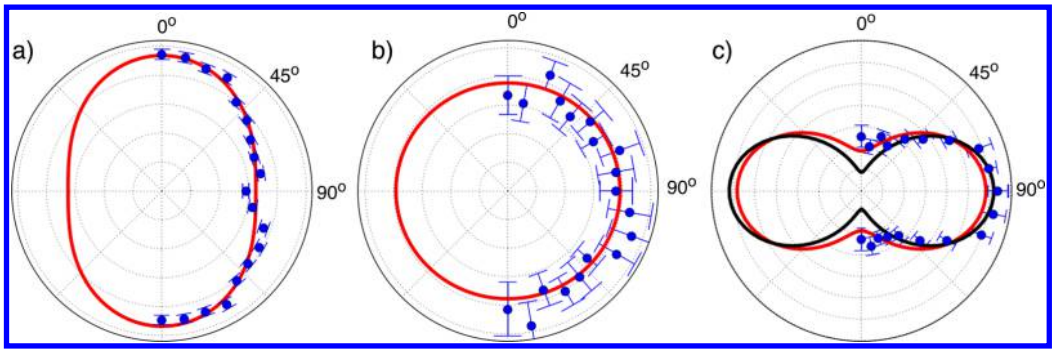

Figure 4. Xe^+ $5p^5 \rightarrow 4d^9 5p^6$ core to valence transitions measured versus the polarization angle at a laser intensity of 1×10^{14} W/cm^2: (a) $^2P_{3/2} \rightarrow {}^2D_{5/2}$, (b) $^2P_{1/2} \rightarrow {}^2D_{3/2}$, and (c) $^2P_{3/2} \rightarrow {}^2D_{3/2}$. The angles represent the polarization difference between the pump and probe laser pulses. Data points were taken every 10°, where $\theta = [0{-}180°]$. The blue dots represent data points, and the red line represents the best-fit line according to eq 1 and the anisotropy parameters reported in Table 2. Error bars on the polar plots correspond to one standard error of the measurement. The solid black line in (c) is the fit by ignoring the data points that are contaminated by nearby spectral peaks (parallel polarized pulses) as described in the text.

Table 2. Experimental Anisotropy Parameters[a]

energy	transition	β_2	β_4
55.4	(Xe^+) $^2P_{3/2} \rightarrow {}^2D_{5/2}$	0.23 ± 0.04	
56.1	(Xe^+) $^2P_{1/2} \rightarrow {}^2D_{3/2}$	−0.03 ± 0.05	
57.4	(Xe^+) $^2P_{3/2} \rightarrow {}^2D_{3/2}$	−0.59 ± 0.04	
56.9	(Xe^{2+}) $^3P_2 \rightarrow {}^1D_2$	0.44 ± 0.06	0.63 ± 0.07
57.1	(Xe^{2+}) $^3P_2 \rightarrow {}^3D_3$	0.64 ± 0.04	0.45 ± 0.04
57.6*	(Xe^{2+}) $^3P_1 \rightarrow {}^3D_2$	−0.70 ± 0.05	0.70 ± 0.06
57.6	(Xe^{2+}) $^1D_2 \rightarrow {}^1F_3$ (Xe^{2+}) $^3P_1 \rightarrow {}^3D_2$	−0.35 ± 0.02	0.41 ± 0.02
59.1	(Xe^{2+}) $^3P_1 \rightarrow {}^3D_1$	−0.65 ± 0.04	0.55 ± 0.05

[a]For Xe^+, all angular information is expressed by β_2, whereas β_4 is required for the Xe^{2+} transitions. Energy is expressed in electronvolts. The measurements for Xe^+ are made at 1×10^{14} W/cm^2, and for Xe^{2+} are at 5×10^{14} W/cm^2. The * at the first instance of 57.6 eV represents the measurement at a laser intensity of 2×10^{14} W/cm^2.

Table 3. Theoretical Basis Set for Describing the Observed Transitions in Xe^{2+}[a]

energy (eV)	transition	σ^*	σ	β_2	β_4
57.1	$^3P_{2,2} \rightarrow {}^3D_3$	1.008	0.690	−1.516	0.535
57.1	$^3P_{2,1} \rightarrow {}^3D_3$	1.008	0.575	1.176	0.200
57.1	$^3P_{2,0} \rightarrow {}^3D_3$	1.008	0.708	2.151	0.693
57.6	$^1D_{2,2} \rightarrow {}^1F_3$	1.305	1.111	−1.516	0.535
57.6	$^1D_{2,1} \rightarrow {}^1F_3$	1.305	1.045	0.790	−1.750
57.6	$^1D_{2,0} \rightarrow {}^1F_3$	1.305	1.116	1.909	2.892
57.6	$^3P_{1,1} \rightarrow {}^3D_2$	0.569	0.623	1.082	0.649
57.6	$^3P_{1,0} \rightarrow {}^3D_2$	0.569	0.538	−1.358	0.344
59.1	$^3P_{1,1} \rightarrow {}^3D_1$	0.248	0.154	1.397	−0.147
59.1	$^3P_{1,0} \rightarrow {}^3D_1$	0.248	0.244	−1.687	0.742

[a]The line strength as determined through FAC[38] (σ^*) for a single electronic transition is shown for comparison, and all other parameters are obtained through numerical integration from eq 7.

conditions. As the laser intensity increases, the measured anisotropy for $^2P_{3/2} \rightarrow {}^2D_{3/2}$ decreases to a minimum ($\beta_2 = -0.50$), suggesting an alignment of [80 : 20], and this is complicated by Xe^{2+} absorption peaks as discussed earlier.

IV.B. Alignment in Doubly Charged Ions, Xe^{2+}. The sequential ionization model predicts strong alignment of the $^3P_2$, $^1D_2$, and $^3P_1$ states of Xe^{2+} ($^1S_0$ and $^1P_0$ cannot be aligned). The basis set to interpret the degree of alignment from the doubly charged ion absorption signals, as constructed from eq 7, is presented in Table 3. The first ionization step ($p^6 \rightarrow p^5$) defines the quantization axis and aligns the ion, and the second ionization ($p^5 \rightarrow p^4$) contribution is limited to a $k = 2$ tensor. The XUV absorption ($p^4 \rightarrow d^9p^5$) yields a $k = 2$ tensor, making the observation a product of two $k = 2$ tensors. The observed anisotropy ($k = 4$) is consistent with absorption spectroscopy involving three electronic transitions originating from an unaligned state.

The feature at 56.9 eV (peak d of Figure 2 and Figure 5a) is attributed to $^3P_2 \rightarrow {}^1D_2$, which constitutes a spin-forbidden transition in LS coupling and cannot be interpreted with this level of theory. It is therefore not analyzed, but the experimental cross sections versus angle are nevertheless presented in Figure 5a. The absorption feature at 57.1 eV is attributed to $^3P_2 \rightarrow {}^3D_3$ and shown in Figure 5b. From the measured anisotropy values of $\beta_2 = 0.44 \pm 0.06$ and $\beta_4 = 0.63 \pm 0.07$, an alignment of $|M_J| = [0 : 1 : 2]$ of [27±6 : 45±11 : 29±0] is extracted, as shown in Figure 5c. For $^3P_2$, the sequential model predicts an orbital alignment ratio of [33 : 53 : 14], in relatively good agreement, and validates the sequential ionization rate model.

The 57.6 eV peak (peak (f) of Figure 2 and Figure 6) is composed of two transitions, of which the $^1D_2 \rightarrow {}^1F_3$ transition has approximately double the XUV oscillator strength of $^3P_1 \rightarrow {}^3D_2$.[32] Unambiguous separation is not possible, as the instrument has insufficient spectral resolution. According to the sequential model, at threshold ionization intensity, $^3P_1$ has 3 times the population, compensating for the difference in oscillator strength and therefore more strongly contributing to the absorption peak. In Figure 6a, the anisotropy of the absorption peak is shown at a threshold laser intensity of 2×10^{14} W/cm^2, where the anisotropy parameters are measured as $\beta_2 = -0.70 \pm 0.05$ and $\beta_4 = 0.70 \pm 0.06$. Assuming that the $^3P_1 \rightarrow {}^3D_2$ transition is the sole contributor to the peak at this intensity, which may be an overestimation, a $^3P_1$ alignment of $|M_J| = [0 : 1]$ of [66±3 : 34±1] is measured. This is in excellent agreement with the sequential ionization rate model, which suggests an alignment of [65 : 35].

The laser intensity was maintained below the appearance of triple ionization, meaning all of the peaks representing isolated doubly ionized transitions present a constant anisotropy. However, due to the difference in energy between $^3P_1$ and $^1D_2$, adjustment of the laser intensity can be used to influence the ratio between $^3P_1$ and $^1D_2$ and therefore the anisotropy

dx.doi.org/10.1021/jp503468u | J. Phys. Chem. A 2014, 118, 8614−8624

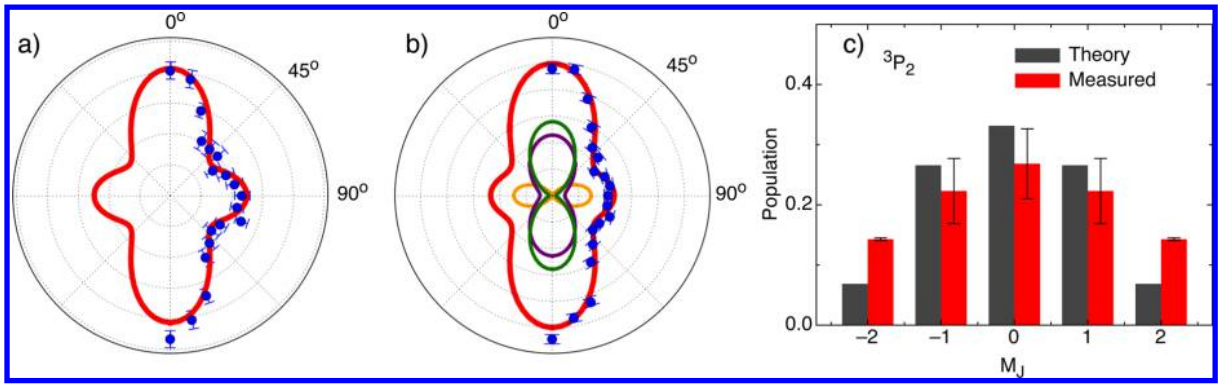

Figure 5. Similar to Figure 4. The Xe^{2+} $5p^4 \rightarrow 4d^95p^5$ absorption transitions measured at a laser intensity of 5×10^{14} W/cm^2. (a) 56.9 eV is assigned to $^3P_2 \rightarrow {}^1D_2$. This peak is not analyzed. (b) 57.1 eV is assigned to $^3P_2 \rightarrow {}^3D_3$. The green line represents the contributions from $M_J = 0$, purple for $M_J = 1$, and gold for $M_J = 2$. (c) The theoretical and experimental orbital populations for $^3P_2$ in (b) are compared. The error bars on the bar charts represent one standard deviation of the fit.

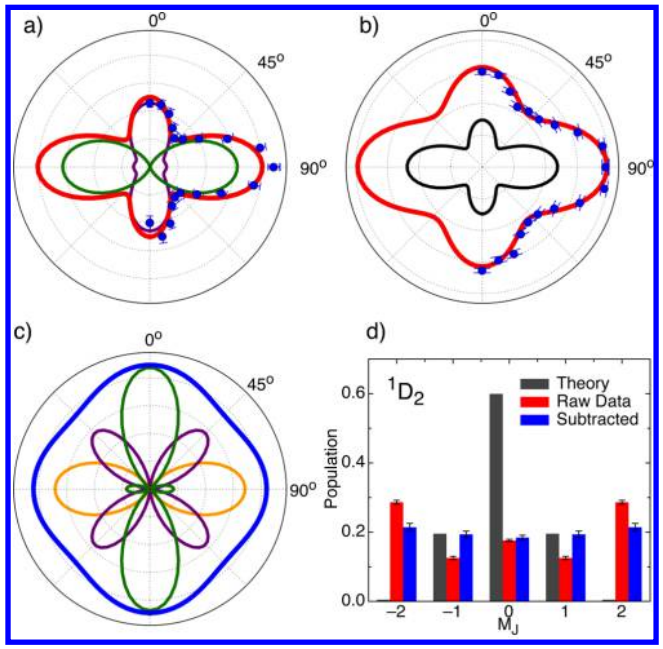

Figure 6. Similar to Figure 5. The Xe^{2+} $5p^4 \rightarrow 4d^95p^5$ absorption measured at 57.6 eV. (a) At low laser intensity of 2×10^{14} W/cm^2, the peak is ascribed to $^3P_1 \rightarrow {}^3D_2$. (b) At a laser intensity of 5×10^{14} W/cm^2, both $^3P_1 \rightarrow {}^3D_2$ and $^1D_2 \rightarrow {}^1F_3$ are present in the signal. The $^1D_2$ populations are fit by assuming two extremes as described in the text. First, the raw signal (red line) is assumed entirely $^1D_2 \rightarrow {}^1F_3$ (fit not shown). The other extreme is assuming equal contributions of both transitions, where the black inset shows the estimated contribution from $^3P_1 \rightarrow {}^3D_2$. (c) After the two lines shown in (b) are subtracted, the remaining signal (blue line) is the estimated contribution of $^1D_2 \rightarrow {}^1F_3$. (d) The theoretical and reconstructed orbital populations for $^1D_2$ are compared. The black bars represent the predictions of the sequential model; red and blue bars represent the $^1D_2 \rightarrow {}^1F_3$ populations fit to the red line of (b) and the blue line in (c), respectively. In (a) and (c) the green line represents the contributions from $M_J = 0$, purple for $M_J = 1$, and gold for $M_J = 2$.

measured for only this peak. As the laser intensity increases, the anisotropy measured at 57.6 eV changes to reflect the growing contribution of the $^1D_2 \rightarrow {}^1F_3$ transition. Figure 6b shows the anisotropy at the highest laser intensities examined 5×10^{14} W/cm^2, where the anisotropy parameters are measured to be $\beta_2 = -0.35 \pm 0.02$ and $\beta_4 = 0.41 \pm 0.02$. At this laser intensity, the populations of $^3P_1$ and $^1D_2$ are predicted to be approximately equivalent by the sequential ionization model, but because the oscillator strength is stronger for $^1D_2$, this state contributes more to the peak. Experimentally, it is not possible to isolate the contribution of $^1D_2 \rightarrow {}^1F_3$, and so the data are fit on the basis of two extreme cases. As an upper limit, the anisotropy is treated as if the peak is entirely attributed to $^1D_2 \rightarrow {}^1F_3$, and an alignment $|M_J| = [0 : 1 : 2]$ of $[18\pm0 : 25\pm1 : 57\pm1]$ is measured. At the other extreme, we remove an overestimated $^3P_1 \rightarrow {}^3D_2$ contribution by subtracting the anisotropy obtained at the threshold intensity and scaled to account for half of the peak, as shown in Figure 6b. Fitting the anisotropy of the remaining peak, the data suggest an alignment in $^1D_2$ of $[18\pm1 : 39\pm2 : 43\pm2]$. Both results indicate an almost complete lack of alignment in the $^1D_2$ state, where an unaligned distribution is $[20 : 40 : 40]$. Although the actual alignment of $^1D_2$ is most likely between these two extremes, it is clear that the results are in poor agreement with the sequential ionization model where a large alignment of $[60 : 39 : 1]$ is predicted. This suggests that the alignment is greatly diminished, and the $M_J = 0$ population is not as prominent as predicted by the sequential ionization model. This is further addressed in the Discussion.

Finally, at laser intensities of 5×10^{14} W/cm^2, a small peak at 59.1 eV is observed as shown in Figure 2, peak g. Although the energy of the p^4 terms are well-known, the d^9p^5 terms are less well characterized and inaccuracies in the calculations of the energy levels resulting from the multielectronic interactions of the open d shell make peak assignments difficult. Atomic calculations predict $^3P_1 \rightarrow {}^3D_1$ at 58.5 eV and $^3P_2 \rightarrow {}^3P_2$ at 59.5 eV,[31] with the first peak being 20%[31] to 55%[38] larger. A previous high resolution photoelectron experiment observed two peaks at 58 and 59 eV and assigned them to these transitions, although the calculated line strengths were not in agreement. Here, an anisotropy of $\beta_2 = -0.65 \pm 0.04$ and $\beta_4 = -0.55 \pm 0.05$ is measured, as presented in Figure 7. The peak at 59 eV was previously assigned as $^3P_2 \rightarrow {}^3P_2$,[32] but the angular distributions cannot account for the observed anisotropy, which may suggest that the previous assignment is incorrect. Instead, we assign the peak to the $^3P_1 \rightarrow {}^3D_1$ transition, which by having a larger cross-section should be more easily observed. An alignment for $^3P_1$ of $|M_J| = [0 : 1]$ of $[56\pm2 : 44\pm2]$ is extracted. This alignment is only slightly lower than predicted by the sequential ionization model. Also shown in Figure 7b is the measured alignment of $^3P_1$ taken at 2×10^{14} W/cm^2 for the peak at 57.6 eV.

dx.doi.org/10.1021/jp503468u | J. Phys. Chem. A 2014, 118, 8614−8624

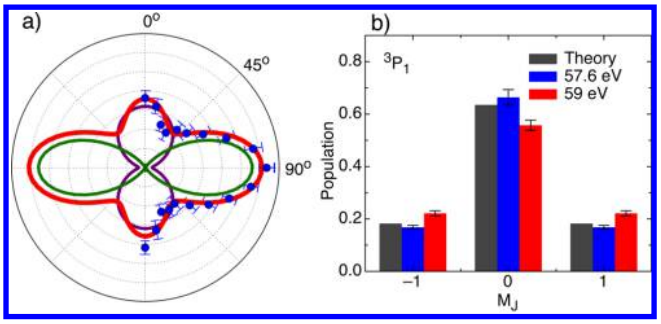

Figure 7. (a) Similar to Figure 5. The Xe^{2+} $5p^4 \rightarrow 4d^95p^5$ absorption peak at 59 eV is attributed to $^3P_1 \rightarrow {}^3D_1$. The green line is attributed to the contribution from the $^3P_{1,0}$ substate and the purple line is from the $^3P_{1,1}$ substate. (b) Comparison of theoretical and measured alignment for $^3P_1$. The black bars are the populations derived from the sequential ionization model, blue bars are measured from the low intensity (2×10^{14} W/cm^2) transition at 57.6 eV as shown in Figure 6a, and red bars are from the plot in this figure at 59 eV at 5×10^{14} W/cm^2.

V. DISCUSSION

Both tunneling ionization and electron-recollision occur due to the interaction of the strong electric field of the laser and the active electron and therefore are not easily separated. As both processes are thought to always be present, a well-defined transition between nonsequential and sequential ionization does not exist. At intensities too low to induce tunnel ionization, electron recollision is believed to be responsible for NSDI. However, at very high laser intensities the recollision is expected to play less of a role, and the sequential ionization rates can account for the ion yields. The sequential ionization model described here ignores the third step of the recollision model and relies on the assumption that once an electron is removed, it no longer interacts with the remaining ion core. The alignment measurements for the triplet states are in general agreement with this level of theory. However, the anisotropy attributed to the $^1D_2$ state represents an almost entirely unaligned distribution and is in poor agreement with the model. Together, these results suggest that the alignment generated by SFI with linearly polarized laser pulses is spin state dependent.

This stark contrast in the agreement between experiment and theory for the alignments of singlets and triplets can be understood by including spin in the rescattering concept. A "hole" is treated as a particle with defined spin and angular momentum that represents the properties of the missing electron. In singlets, where the two holes have an orthogonal spin direction, they may occupy the same final atomic orbital. In triplets, both holes have identical spin directions and cannot occupy the same space due to the Pauli exclusion principle, and therefore, they must reside in different final orbitals. The experimental results suggest that for linearly polarized light, the probability for the liberated electron to return to and impact with its parent orbital is large, diminishing the alignment in the process of forming singlet states. In contrast, the probability for recollision with a different atomic orbital may not be as significant for linearly polarized light, which allows the sequential tunnel ionization rates to determine the alignment of triplet states.[47,48] Therefore, although the effects from electron recollision and NSDI can be ignored in triplet spin states, their influence is strong in singlet spin states over the intensity range where these experiments are performed. The difference between singlet and triplet final state alignment in strong-field double ionization provides a new window on electron correlation phenomena.

The alignment measured here for Xe^+ is in excellent agreement with the sequential ionization model. Testing the sequential model with various laser pulse parameters does not explain the reduced alignment observed in previous experiments. However, the alignment is prepared not only by the anisotropy of laser-atom interaction but also by scattering introduced through the electron−ion recollision. Consider two laser pulses of equal peak intensity but contrasting pulse width. For long laser pulses, electron tunneling is most probable at the very peak of the electric field as intensity slowly increases during the leading edge of the pulse envelope. The intensity of each subsequent laser half-cycle increases only slightly meaning the electron has little or no kinetic energy when returning to the ion and therefore may not significantly influence the alignment. However, for very short, few-cycle pulses, the laser intensity increases so abruptly that tunneling occurs away from the field's peak, and the phase of the laser at the time of ionization becomes important. The subsequent half-cycle can have significantly higher amplitude and therefore return the electron with large kinetic energy (up to 3.2^1 times the ponderomotive potential of the laser field). This energetic impact can randomize the orbital alignment in the final state of the ion. This predicts alignment to be in better agreement for longer pulses, which matches the literature trend. A complete description of the scattering event requires accounting for the nonlinearity of the electric field, Coulomb interaction between electrons, and a well-characterized laser pulse.

The orbital alignment in Xe^{2+} may be strongly dependent on the polarization parameters of the laser and the prospect of controlling the state alignment warrants further investigation. Recollision is not expected when circularly polarized light is driving the ionization, and therefore it may be investigated if such parameters can be used to prepare aligned singlet states. With elliptically polarized light, it may also be possible to enhance the recollision into other atomic orbitals and therefore influence the alignment in triplet states, or even prepare an orientation in the quantum state distribution. The small disagreements between experiment and theory for the triplet states might be considered in terms of the coherent electron motion that occurs in the ion during the time between where the electrons tunnel or recollide with the ion. Tracing the motion of electrons on the attosecond time scale, by using laser pulses of duration less than or comparable to the spin−orbit period, will reveal additional details regarding the multielectronic effects during ionization. Gaining a better understanding of electron correlation effects has important consequences for further developing SFI for the measurement of the electronic properties of molecules, clusters, and solid state materials, which is essential to understanding attosecond wave packet formation and propagation.

VI. CONCLUSIONS

The alignment prepared through the strong-field single and double ionization of xenon has been measured using core−hole absorption spectroscopy. For singly charged ions, an almost perfect alignment was recorded in $^2P_{3/2}$, with the hole occupying the $|M_J| = 1/2$ substate, in excellent agreement with theory. The anisotropy of Xe^{2+} transitions $4d^{10}5p^4 \rightarrow 4d^95p^5$ were quantified in terms of multipole expansion parameters, β_2 and β_4. From the anisotropy, the alignment of

dx.doi.org/10.1021/jp503468u | J. Phys. Chem. A 2014, 118, 8614−8624

the p^4 terms were extracted and used to reveal the role of electron correlation in the alignment prepared through the strong-field double ionization of noble gas atoms. For the triplet spin states, the recorded alignment is in good agreement with the sequential ionization rate model. However, although the sequential ionization model predicts a strong alignment in the singlet spin state ($^1D_2$), the experimental data suggest that the state is nearly unaligned. We attribute the loss of alignment in the singlet to electron−ion recollision that occurs during NSDI. For linearly polarized laser pulses the electron−ion recollision occurs in singlet spin states more prominently than in triplet spin states. Our results imply that alignment generated through strong-field double ionization is spin-state dependent, and dynamical calculations may reveal a broader context for spin dependence in these processes.

AUTHOR INFORMATION

Corresponding Author

*S. R. Leone: e-mail, srl@berkeley.edu; tel, (510) 643-5467; fax, (510) 643-1376.

Author Contributions

The manuscript was written through contributions of all authors. All authors have given approval to the final version of this manuscript.

Notes

The authors declare no competing financial interest.

ACKNOWLEDGMENTS

We thank A. N. Pfeiffer for fruitful discussions. S.G.S. is supported by the National Science Foundation Chemistry Division CHE-1049946. E.R.H. and S.R.L. acknowledge support from the National Science Foundation Engineering Research Center for Extreme Ultraviolet Science and Technology Grant No. EEC-0310717. Funding for materials and equipment was provided through the Department of Energy Grant No. DE-AC02-05-CH11231 via the LBNL Chemical Sciences Division. S.R.L. acknowledges additional support that contributed to the intellectual content of this project: W.M. Keck Foundation; Department of Defense National Security Science and Engineering Faculty Fellowship.

REFERENCES

(1) Corkum, P. B. Plasma Perspective on Strong-field Multiphoton Ionization. *Phys. Rev. Lett.* **1993**, *71*, 1994.

(2) Paul, P. M.; Toma, E. S.; Breger, P.; Mullot, G.; Augé, F.; Balcou, P.; Muller, H. G.; Agostini, P. Observation of a Train of Attosecond Pulses from High Harmonic Generation. *Science* **2001**, *292*, 1689−1692.

(3) Itatani, J.; Levesque, J.; Zeidler, D.; Niikura, H.; Pépin, H.; Kieffer, J. C.; Corkum, P. B.; Villeneuve, D. M. Tomographic Imaging of Molecular Orbitals. *Nature* **2004**, *432*, 867−871.

(4) Shafir, D.; Mairesse, Y.; Villeneuve, D. M.; Corkum, P. B.; Dudovich, N. Atomic Wavefunctions Probed Through Strong-Field Light−Matter Interaction. *Nat. Phys.* **2009**, *5*, 412−416.

(5) Tallents, G.; Wagenaars, E.; Pert, G. Lithography at EUV Wavelengths. *Nat. Photonics* **2010**, *4*, 809−811.

(6) Goulielmakis, E.; Loh, Z.-H.; Wirth, A.; Santra, R.; Rohringer, N.; Yakovlev, V. S.; Zherebtsov, S.; Pfeifer, T.; Azzeer, A. M.; Kling, M. F.; et al. Real-Time Observation of Valence Electron Motion. *Nature* **2010**, *466*, 739−744.

(7) Lépine, F.; Ivanov, M. Y.; Vrakking, M. J. J. Attosecond Molecular Dynamics: Fact or Fiction? *Nat. Photonics* **2014**, *8*, 195−204.

(8) Hosler, E. R.; Leone, S. R. Charaterization of Vibrational Wave Packets by Core-Level High-Harmonic Transient Absorption Spectroscopy. *Phys. Rev. A* **2013**, *88*, 023420.

(9) Ammosov, M. V.; Delone, N. B.; Krainov, V. P. Tunnel Ionization of Complex Atoms and Atomic Ions by an Alternating Electromagnetic Field. *Sov. Phys. JETP* **1986**, *64*, 1191−1194.

(10) Sayres, S. G.; Ross, M. W.; Castleman, A. W., Jr. Influence of Clustering and Molecular Orbital Shapes on the Ionization Enhancement in Ammonia. *Phys. Chem. Chem. Phys.* **2011**, *13*, 12231.

(11) Sayres, S. G.; Ross, M. W.; Castleman, A. W., Jr. Onset of Coulomb Explosion in Small Silicon Clusters Exposed to Strong-Field Laser Pulses. *New J. Phys.* **2012**, *14*, 055014.

(12) Sansone, G.; Pfeifer, T.; Simeonidis, K.; Kuleff, A. I. Electron Correlation in Real Time. *ChemPhysChem* **2012**, *13*, 661−680.

(13) Zhou, Y.; Huang, C.; Tong, A.; Liao, Q.; Lu, P. Correlated Electron Dynamics in Nonsequential Double Ionization by Orthogonal Two-Color Laser Pulses. *Opt. Express* **2011**, *19*, 2301−2308.

(14) Sukiasyan, S.; McDonald, C.; Destefani, C.; Ivanov, M. Y.; Brabec, T. Multielectron Correlation in High-Harmonic Generation: A 2D Model Analysis. *Phys. Rev. Lett.* **2009**, *102*, 223002.

(15) Zhao, Z.; Wu, J.; Yuan, J. Toward Tomographic Imaging of Singlet and Triplet States Using High-Order Harmonic Generation. *J. Phys. B: At., Mol. Opt. Phys.* **2008**, *41*, 155601.

(16) Fittinghoff, D. N.; Bolton, P. R.; Chang, B.; Kulander, K. C. Observation of Nonsequential Double Ionization of Helium with Optical Tunneling. *Phys. Rev. Lett.* **1992**, *69*, 2642−2645.

(17) Fleischer, A.; Wörner, H. J.; Arissian, L.; Liu, L. R.; Meckel, M.; Rippert, A.; Dörner, R.; Villeneuve, D. M.; Corkum, P. B.; Staudte, A. Probing Angular Correlations in Sequential Double Ionization. *Phys. Rev. Lett.* **2011**, *107*, 113003.

(18) Pfeiffer, A. N.; Cirelli, C.; Smolarski, M.; Dörner, R.; Keller, U. Timing the Release in Sequential Double Ionization. *Nat. Phys.* **2011**, *7*, 428−433.

(19) Bryon, W. A.; Stebbings, S. L.; English, E. M. L.; Goodworth, T. R. J.; Newell, W. R.; McKenna, J.; Suresh, M.; Srigengan, B.; Williams, I. D.; Turcu, I. C. E.; et al. Geometry- and Diffraction-Independent Ionization Probabilities in Intense Laser Fields: Probing Atomic Ionization Mechanisms with Effective Intensity Matching. *Phys. Rev. A* **2006**, *73*, 013407.

(20) Hansch, P.; Walker, M. A.; Woerkom, L. D. V. Spatially Dependent Multiphoton Multiple Ionization. *Phys. Rev. A* **1996**, *54*, R2559−R2562.

(21) Young, L.; Arms, D. A.; Dufresne, E. M.; Dunford, R. W.; Ederer, D. L.; Höhr, C.; Kanter, E. P.; Krässig, B.; Landhal, E. C.; Peterson, E. R.; et al. X-ray Microprobe of Orbital Alignment in Strong-Field Ionized Atoms. *Phys. Rev. Lett.* **2006**, *97*, 083601.

(22) Southworth, S. H.; Arms, D. A.; Dufresne, E. M.; Dunford, R. W.; Ederer, D. L.; Höhr, C.; Kanter, E. P.; Krässig, B.; Landahl, E. C.; Peterson, E. R.; et al. K-edge X-ray Absorption Spectroscopy of Laser Generated Kr^+ and Kr^{2+}. *Phys. Rev. A* **2007**, *76*, 043421.

(23) Loh, Z.-H.; Khalil, M.; Correa, R. E.; Santra, R.; Buth, C.; Leone, S. R. Quantum State-Resolved Probing of Strong-Field-Ionized Xenon Atoms Using Femtosecond High-Order Harmonic Transient Absorption Spectroscopy. *Phys. Rev. Lett.* **2007**, *98*, 143601.

(24) Lin, M.-F.; Pfeiffer, A. N.; Neumark, D. M.; Leone, S. R.; Gessner, O. Strong-field Induced XUV Transmission and Multiplet Splitting in 4d-6p Core-Excited Xe Studied by Femtosecond XUV Transient Absorption Spectroscopy. *J. Chem. Phys.* **2012**, *137*, 244305.

(25) Rohringer, N.; Santra, R. Multichannel Coherence in Strong-Field Ionization. *Phys. Rev. A* **2009**, *79*, 053402.

(26) Loh, Z.-H.; Leone, S. R. Capturing Ultrafast Quantum Dynamics with Femtosecond and Attosecond X-ray Core-Level Absorption Spectroscopy. *J. Phys. Chem. Lett.* **2012**, *4*, 292−302.

(27) Wirth, A.; Santra, R.; Goulielmakis, E. Real Time Tracing of Valence-Shell Electronic Coherences With Attosecond Transient Absorption Spectroscopy. *Chem. Phys.* **2013**, *414*, 149−159.

(28) Shiner, A. D.; Schmidt, B. E.; Trallero-Herrero, C.; Wörner, H. J.; Patchkovskii, S.; Corkum, P. B.; Kieffer, J.-C.; Légaré, F.; Villeneuve,

D. M. Probing Collective Multi-Electron Dynamics in Xenon With High-Harmonic Spectroscopy. *Nat. Phys.* **2011**, *7*, 464−467.
(29) Pfeiffer, A. N.; Sayres, S. G.; Leone, S. R. Calculation of Valence Electron Motion Induced by Sequential Strong-Field Ionisation. *Mol. Phys.* **2013**, *111*, 2283−2291.
(30) Loh, Z. H.; Khalil, M.; Correa, R. E.; Leone, S. R. A Tabletop Femtosecond Time-Resolved Soft X-ray Transient Absorption Spectrometer. *Rev. Sci. Instrum.* **2008**, *79*, 073101.
(31) Koizumi, T.; Awaya, Y.; Fujino, A.; Itoh, Y.; Kitajima, M.; Kojima, T. M.; Oura, M.; Okuma, R.; Sano, M.; Seikioka, T.; et al. 4d Photoionization of Multiply Charged Xe^{q+}(q = 1−3) Ions. *Phys. Scr.* **1997**, *T73*, 131−132.
(32) Anderson, P.; Anderson, T.; Folkmann, F.; Ivanov, V. K.; Kjeldsen, H.; West, J. B. Absolute Cross Sections for the Photoionization of 4d Electrons in Xe^{+} and Xe^{2+} Ions. *J. Phys. B: At., Mol. Opt. Phys.* **2001**, *34*, 2009−2019.
(33) Ederer, D. L.; Manalis, M. Photoabsorption of the 4d Electrons in Xenon. *J. Opt. Soc. Am.* **1975**, *65*, 634−637.
(34) Tong, X. M.; Lin, C. D. Empirical Formula for Static Field Ionization Rates of Atoms and Molecules by Lasers in the Barrier-Suppression Regime. *J. Phys. B: At. Mol. Opt. Phys.* **2005**, *38*, 2593−2600.
(35) Cowan, R. D. *The Theory of Atomic Structure and Spectra*; University of California Press: Oakland, CA, 1981.
(36) Wörner, H. J.; Corkum, P. B. Imaging and Controlling Multielectron Dynamics by Laser-Induced Tunnel Ionization. *J. Phys. B: At., Mol. Opt. Phys.* **2011**, *44*, 041001.
(37) NIST Atomic Spectra Database, http://physics.nist.gov/asd.
(38) Gu, M. F. The Flexible Atomic Code. *Can. J. Phys.* **2008**, *86*, 675−689.
(39) Case, D. A.; McClelland, G. M.; Herschbach, D. R. Angular Momentum Polarization in Molecular Collisions: Classical and Quantum Theory for Measurements Using Resonance Fluorescence. *Mol. Phys.* **1978**, *35*, 541−573.
(40) Gâcon, J. C.; Marcerou, J. F.; Bouazaoui, M.; Jacquier, B.; Kibler, M. Two-Photon Transition Intensities for Sm^{2+} in BaClF. *Phys. Rev. B* **1989**, *40*, 2070−2075.
(41) Kummel, A. C.; Sitz, g. O.; Zare, R. N. Determination of Population and Alignment of the Ground State Using Two-Photon Nonresonant Excitation. *J. Chem. Phys.* **1986**, *85*, 6874−6897.
(42) Greene, C. H.; zare, R. N. Photofragment Alignment and Orientation. *Annu. Rev. Phys. Chem.* **1982**, *33*, 119−150.
(43) Greene, C. H.; Zare, R. N. Determination of Product Population and Alignment Using Laser-Induced Fluorescence. *J. Chem. Phys.* **1983**, *78*, 6741−6753.
(44) Robinson, R. L.; Kovalenko, L. J.; Smith, C. J.; Leone, S. R. Individual Cross Sections for $^1D_2$ Sublevels (M_L = 0,1,2) in the Alignment-Dependent Process: $Ca(4p^2\ ^1D_2) + Rg \rightarrow Ca(3d4p\ ^1F_3) + Rg$ as a Function of Rare Gas. *J. Chem. Phys.* **1990**, *92*, 5260−5269.
(45) Lin, Y. F.; Yak, L.; Lee, S. K.; Herath, T.; Li, W. Orbital Alignment in Photodissociation Probed Using Strong Field Ionization. *J. Chem. Phys.* **2011**, *135*, 234311.
(46) Watanabe, D.; Ohoyama, H.; Matsuma, T.; Kasai, T. Steric Effect in the Energy Transfer Reaction of $Ar(^3P_2) + N_2$. *J. Chem. Phys.* **2006**, *125*, 084316.
(47) Ruiz, C.; Plaja, L.; Roso, L. Ionization of Lithium in a Strong Laser Field. *Laser Physics* **2006**, *16*, 600−606.
(48) Tew, D. P.; Klopper, W.; Helgaker, T. Electron Correlation: The Many-Body Problem at the Heart of Chemistry. *J. Comput. Chem.* **2007**, *28*, 1307−1320.